Boundary-Layer Meteorol (2015) 157:23–43
DOI 10.1007/s10546-015-0045-5

NOTES AND COMMENTS

An Extension of the Mellor–Yamada Model to the Terra Incognita Zone for Dry Convective Mixed Layers in the Free Convection Regime

Junshi Ito[1,2] · Hiroshi Niino[1] · Mikio Nakanishi[3] · Chin-Hoh Moeng[4]

Received: 11 November 2014 / Accepted: 14 May 2015 / Published online: 16 June 2015

Abstract The terra incognita (TI) or grey zone arises in conventional planetary boundary-layer parametrizations when the grid resolution of a numerical model is comparable to the size of the energy-containing turbulent eddies ∼1 km or less. Here, we investigate a simple, plausible extension of the Mellor–Yamada (MY) level-3 scheme for TI-scale grid size using a large-eddy simulation (LES) as a benchmark. Horizontal filtering of the benchmark simulation data for the dry convective mixed layer in the free convection regime yields subfilter-scale components whose statistics are then retrieved for various filter sizes. This leads to a modified MY level-3 scheme for TI-scale grid sizes. The proposed TI scheme incorporates: (1) modification of various length scales in the conventional MY scheme by an empirical function that depends on the horizontal grid size normalized by the convective boundary-layer height; (2) a new length scale for horizontal turbulent fluxes; and (3) a linear relationship between the local dissipation length and subfilter-scale turbulent kinetic energy. A posteriori tests of the proposed TI scheme show a much improved performance compared with the conventional MY level-3 scheme. The ratio of the grid-scale to the subgrid-scale turbulent intensity is comparable to that obtained from the filtered LES solutions. Sensitivity tests show that the modification of the dissipation length scales has the largest impact, while the new length scale for horizontal fluxes also proves important. A simulation that includes all of the above modifications results in the optimum performance.

Keywords Grey zone · Horizontal resolution · Mellor–Yamada model · Terra incognita · Turbulence parametrization

✉ Junshi Ito
junshi@aori.u-tokyo.ac.jp

1 Atmosphere and Ocean Research Institute, The University of Tokyo, 5-1-5 Kashiwanoha, Kashiwa, Chiba 277-8564, Japan

2 Present Address: Meteorological Research Institute, Japan Meteorological Agency, 1-1 Nagamine, Tsukuba, Ibaraki 305-0052, Japan

3 National Defense Academy, Yokosuka, Japan

4 National Center for Atmospheric Research, Boulder, USA

1 Introduction

Turbulent eddies contribute significantly to the vertical exchanges of momentum, heat, and moisture in the atmospheric boundary layer. These eddies are not typically resolved by conventional numerical weather prediction (NWP) models, and so the net effects of the eddies are usually parametrized using ensemble mean turbulence closure schemes. Stull (1988) reviews various parametrization schemes for turbulent fluxes.

The Mellor–Yamada (MY) scheme (Mellor and Yamada 1982) is a widely used parametrization in NWP models with the advantage of its flexibility in systematically reducing the number of prognostic variables in the set of second-moment equations. The full MY level-4 scheme needs 11 prognostic second-moment variables (for a dry atmosphere), but only two are retained in the level-3 scheme. Further simplification leads to a single prognostic equation for turbulent kinetic energy (TKE) for level-2.5 and none for level-2. Because it is theoretically based on the moment equations and has reduced computational cost, the MY level-3 (or lower) scheme is often used to represent the planetary boundary layer (PBL) in mesoscale and global-scale NWP models. For example, the Japan Meteorological Agency (JMA) now employs a modified MY level-3 PBL scheme (Nakanishi and Niino 2006) for their operational regional NWP model (JMA non-hydrostatic model; Saito et al. 2007).

Advances in computational power now enable NWP models to adopt horizontal grid resolutions on the order of 1 km, which is comparable to the size of energy-containing turbulent eddies in the atmospheric convective boundary layer (CBL). A finer grid resolution is favourable because NWP models can better resolve complex terrain and hence improve forecast skill (e.g., Leroyer et al. 2014); for example, a realistic formation of roll clouds in a cold-air outbreak was simulated by the JMA non-hydrostatic model using a fine horizontal grid size of 1 km (Eito et al. 2004). However, a new problem, termed the "terra incognita" (TI) by Wyngaard (2004) or grey zone, arises in turbulence parametrizations with finer horizontal grid resolutions. With a TI grid resolution, turbulent transports are partly resolved, which violates the basis of conventional (ensemble-mean) parametrizations.

A number of studies have focused on parametrizing turbulence for TI grid scales. For example, a TI scheme has been developed and implemented in the regional model of the UK Meteorological Office (Boutle et al. 2014) based on their non-local turbulence scheme; Shin and Hong (2014) have also proposed an extension to the non-local YSU scheme (Hong et al. 2006); Kitamura (2015) has proposed an extension to the Deardorff model (Deardorff 1980). For NWP models that are based on higher-order closure schemes, Ramachandran and Wyngaard (2011) have proposed the use of a full set of second-moment conservation equations, similar to the MY level-4 scheme, to resolve the TI problem. However, a large increase in the number of prognostic moment equations in the PBL scheme is computationally expensive and hence not practical for NWP purposes.

The present study proposes a simple extension of the MY level-3 (or lower) scheme for NWP models with a TI grid resolution. This extension adjusts the length scale, which is a free parameter, as attempted in previous studies (Cuxart et al. 2000; Beare 2014). We consider the case of a thermally unstable CBL in the free convection regime in which the transport of momentum is insignificant for turbulence structures and moisture is absent. In this case, the TI problem is more likely to arise because the energy-containing turbulent eddies are of the size of the CBL depth (on the order of 1 km).

Here, we use a large-eddy simulation (LES) as a benchmark, as in previous studies (Honnert et al. 2011; Shin and Hong 2013; Zhou et al. 2014), to investigate the representation of CBL turbulence in NWP models with a TI-zone grid mesh. We apply horizontal filtering to

the benchmark simulations using filter scales that correspond to various TI scales to separate the LES flow fields into resolvable and subgrid-scale (SGS) components. The SGS statistics are then analyzed to examine their dependence on the TI scale.

The remainder of the paper is organized as follows: Sect. 2 describes the benchmark LES and post-processing methodology, and briefly reviews the MY PBL scheme. Section 3 presents the a priori analysis for the TI scale based on the benchmark LES, and proposed modifications are tested (i.e. a posteriori test) and discussed in Sect. 4. Section 5 presents our conclusions.

2 Large-Eddy Simulations and Post-processing Methodology

2.1 Large-Eddy Simulations

The three-dimensional LES model employed in the present study has been used by Nakanishi and Niino (2004) and Ito et al. (2013), and employs the Boussinesq approximation and Smagorinsky's SGS model on the Arakawa C-grid. A uniform grid size of 25 m in all three dimensions is used, where the horizontal domain is 18 km $\times$ 18 km, and the vertical extent is 5 km. The top boundary is free-slip and adiabatic, while the lateral boundaries are cyclic. No ambient wind is included in the control runs. The initial potential temperature increases linearly with height from a surface value of 299 K and with a vertical gradient, Γ, of 4 K km^{-1}. We performed two LES control runs with constant kinematic heat fluxes of $Q = 0.2$ and 0.1 K m s^{-1} imposed at the surface. The surface stress is calculated using a bulk method based on the Monin–Obukhov similarity law with the non-dimensional gradient functions of Businger et al. (1971). White noise of small amplitude is added to the entire calculation domain to initiate convection. Time integration is performed with a timestep of 0.2 s for a 20-h period.

The CBL grows continuously owing to the positive surface heat flux Q, and the time evolution of the CBL height h, convective velocity scale w_* and temperature scale θ_* are shown in Fig. 1a–c, where h is determined from the maximum gradient of potential temperature θ, $w_* \equiv (ghQ/\theta_0)^{1/3}$, θ_0 is the reference potential temperature and $\theta_* = Q/w_*$. Figure 1d shows a horizontal (x- and y-) cross-section of the simulated vertical velocity field at a height $z = 0.5h$ at $t = 5$ h. The structure of convection is similar to that described in the literature, and various statistics scale well with the free convection scales (Deardorff 1970) h, w_*, θ_*, and the eddy turnover time h/w_*.

Figure 1e shows the vertical profiles of production, dissipation, and turbulent and pressure transport from the LES, averaged over the whole numerical domain and normalized by free convection scaling at $t = 5$ h. These profiles quantitatively agree with the results of other LES studies (e.g., Moeng and Sullivan 1994).

2.2 Horizontal Filtering and Scaling

The grid-point values in the LES solutions are filtered and decomposed into filter scale (FS) and sub-filter scale (SFS) components with respect to a filter size Δ_H. The filter-scale value of a variable ϕ is defined as

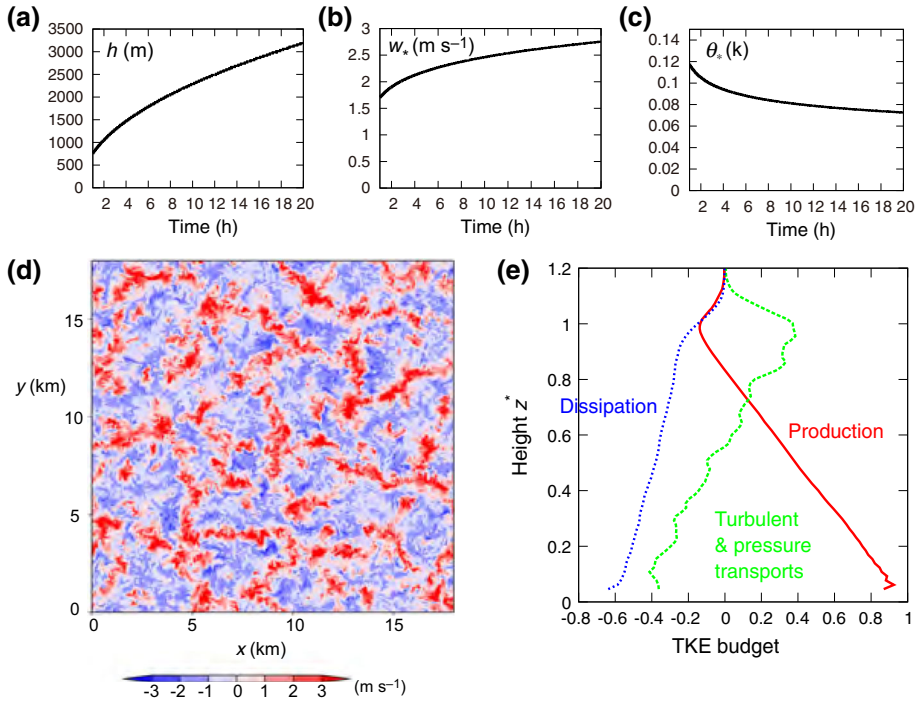

Fig. 1 Results of the benchmark LES: **a**–**c** time series of h, w_* and θ_*, respectively; **d** horizontal cross-section of vertical velocity at $z = 0.5h$ and $t = 5$ h; **e** vertical profiles of horizontally-averaged production, dissipation, and turbulent and pressure transport of TKE at $t = 5$ h

$$\bar{\phi}(\mathbf{x}') = \frac{1}{{\Delta_H}^2} \int_{y-\Delta_H/2}^{y+\Delta_H/2} \int_{x-\Delta_H/2}^{x+\Delta_H/2} \phi(\mathbf{x}') \mathrm{d}x' \mathrm{d}y', \tag{1}$$

where the overbar denotes a spatial top-hat filter in the x and y directions. Figure 2a demonstrates the filtering operation for $\Delta_H = 125$ m as an example. The SFS is defined as deviations from the filter-scale value at the centre of that filter box; i.e., $\phi'(x, y) = \phi(x, y) - \bar{\phi}(x, y)$. For convenience, we omit the prime in the symbols for SFS representation hereafter. We have ignored the LES SGS contribution because it is much smaller than that of the scales resolved by the LES in the TI zone. Accordingly, the SFS horizontal heat flux, for example, is computed as $f_x = \overline{u\theta} - \bar{u}\bar{\theta}$ where θ is the potential temperature deviation from θ_0.

In addition to the free convection scaling, we also introduce a non-dimensional filter scale $\Delta_H^* (\equiv \Delta_H / h)$; note that $\Delta_H^* \sim 1$ corresponds to the TI scale, i.e., the filter size is on the order of the PBL depth.

The horizontal average (represented by angle brackets) of the magnitude of the SFS horizontal heat fluxes $\langle |f_x| \rangle$ for various Δ_H^* at three heights is shown in Fig. 2b; for moderate $\Delta_H^* \sim 1$, $\langle |f_x| \rangle$ is a decreasing function of Δ_H^* and becomes small for larger Δ_H^* and consistent with field observations (Wyngaard et al. 1971), because there is no mean gradient of temperature in the x or y directions (mesoscale limit). For small Δ_H^*, on the other hand, $\langle |f_x| \rangle$ decreases with decreasing Δ_H^* because most turbulent transport occurs at the grid scale (LES limit). The peak value of $\langle |f_x| \rangle$ occurs near the TI scale where heterogeneity of convection cells is apparent in the filter scale unlike the mesoscale limit, but the SFS contain

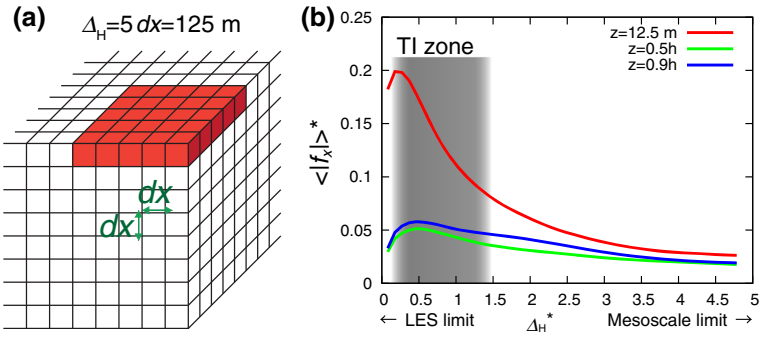

Fig. 2 **a** Schematic picture of the filtering operation in the case of $\Delta_H = 125$ m, and **b** magnitude of the filtered horizontal heat flux $\langle |f_x| \rangle^*$ for various Δ_H^* at the lowest level, $z^* = 0.5$, and $z^* = 0.9$ at 5 h

significant fluxes unlike the LES limit. This suggests that a filter size around the peak value, in the range of $0.2 < \Delta_H^* < 1.5$, can be considered as the TI zone.

2.3 The Conventional Mellor–Yamada Scheme

Here, we describe the governing equations of the improved MY (MYNN) level-3 scheme, where notations follow Nakanishi and Niino (2009) unless specified otherwise. One could use the ensemble average in mesoscale modelling including the MY scheme. While the ensemble and spatial averages defined by Eq. 1 are fundamentally different as discussed in Wyngaard (2004), the spatial average is expected to be close to the ensemble average at the mesoscale limit (Wyngaard 2004). We assume the spatial average instead of the ensemble average in the present study.

The prognostic equation for SFS TKE $e = (\overline{u_i^2} - \bar{u}_i\bar{u}_i)/2$ is

$$\frac{\partial e}{\partial t} = -\bar{u}_i \frac{\partial e}{\partial x_i} - \frac{\partial}{\partial x_i}(\overline{u_i^2 u_j} - 2\bar{u}_i\overline{u_i u_j} - \overline{u_i^2}\bar{u}_j + 2\bar{u}_i{}^2\bar{u}_j) - \frac{\partial}{\partial x_i}\left(\frac{1}{\rho_0}(\overline{u_i p} - \bar{u}_i\bar{p})\right) - \tau_{ij}\frac{\partial u_i}{\partial x_j} + \frac{g}{\theta_0} f_z - \epsilon, \tag{2}$$

where the first term on the right-hand side (r.h.s.) is advection, the second is turbulent transport, the third is pressure transport, the fourth is shear production, the fifth is buoyancy production and the sixth is dissipation. Here, $\tau_{ij} \equiv \overline{u_i u_j} - \bar{u}_i\bar{u}_j - 2/3\delta_{ij}e$ are turbulent fluxes of momentum (deviatoric kinematic Reynolds stress tensor), and f_z is the SFS (kinematic) vertical heat flux. A down-gradient assumption is used to parametrize turbulent and pressure transport (diffusion) fluxes, viz.

$$\overline{u_i^2 u_j} - 2\bar{u}_i\overline{u_i u_j} - \overline{u_i^2}\bar{u}_j + 2\bar{u}_i{}^2\bar{u}_j + \frac{1}{\rho_0}(\overline{u_i p} - \bar{u}_i\bar{p}) = -Lq S_q \frac{\partial e}{\partial x_i}, \tag{3}$$

and dissipation ϵ is parametrized as

$$\epsilon = \frac{q^3}{B_1 L}, \tag{4}$$

where L is a master length scale, B_1 is a closure constant, and q is a turbulent velocity scale defined as $q \equiv \sqrt{2e}$. Temperature variance is also solved prognostically as

$$\frac{\partial(\overline{\theta^2} - \bar{\theta}^2)}{\partial t} = -\bar{u}_i \frac{\partial(\bar{\theta}^2 - \bar{\theta}^2)}{\partial x_i} - \frac{\partial(\overline{u_i\theta^2} - \bar{u}_i\overline{\theta^2} - 2f_i\bar{\theta})}{\partial x_i} - 2f_i\frac{\partial\bar{\theta}}{\partial x_i} - 2\chi, \tag{5}$$

where the first term on the r.h.s. is advection, the second is turbulent transport (diffusion), the third is buoyancy production, and the fourth is dissipation. The turbulent transport in Eq. 5 is parametrized as a down-gradient form,

$$\overline{u_i\theta^2} - \bar{u}_i\overline{\theta^2} - 2f_i\bar{\theta} = -LqS_\theta \frac{\partial(\overline{\theta^2} - \bar{\theta}^2)}{\partial x_i}, \tag{6}$$

whereas dissipation χ is parametrized as

$$\chi = \frac{q(\overline{\theta^2} - \bar{\theta}^2)}{B_2 L}, \tag{7}$$

where B_2 is another closure constant.

The MY level-3 scheme reduces the considerable number of prognostic equations required in the level-4 model by assuming local equilibrium in the turbulent flux budgets. Thus, the budget of τ_{ij} is simplified to a local balance between production, buoyancy, and pressure correlation,

$$\begin{aligned}
&\frac{1}{3}q^2\Big(\frac{\partial\bar{u}_i}{\partial x_j} + \frac{\partial\bar{u}_j}{\partial x_i}\Big) - \Big(\tau_{ik}\frac{\partial\bar{u}_j}{\partial x_k} + \tau_{jk}\frac{\partial\bar{u}_i}{\partial x_k} - \frac{1}{3}\delta_{ij}\tau_{kl}\Big(\frac{\partial\bar{u}_k}{\partial x_l} + \frac{\partial\bar{u}_l}{\partial x_k}\Big)\Big)\\
&\quad + \frac{g}{\theta_0}\Big(\delta_{jz}f_i + \delta_{iz}f_j - \Big(\frac{2}{3}\Big)\delta_{ij}f_z\Big)\\
&\quad + \frac{1}{\rho}\Big(\overline{p\Big(\frac{\partial u_i}{\partial x_j} + \frac{\partial u_j}{\partial x_i}\Big)} - \bar{p}\Big(\frac{\partial\bar{u}_i}{\partial x_j} + \frac{\partial\bar{u}_j}{\partial x_i}\Big)\Big) = 0,
\end{aligned} \tag{8}$$

where only the pressure correlation has to be parametrized. The parametrized pressure correlation consists of slow and rapid parts, and while the slow part works as a sink due to the return-to-isotropy, the rapid part represents the interaction with mean shear and buoyancy,

$$\begin{aligned}
\frac{1}{\rho}\Big(\overline{p\Big(\frac{\partial u_i}{\partial x_j} + \frac{\partial u_j}{\partial x_i}\Big)} - \bar{p}\Big(\frac{\partial\bar{u}_i}{\partial x_j} + \frac{\partial\bar{u}_j}{\partial x_i}\Big)\Big) &= \frac{q}{3A_1L}\tau_{ij} + C_1q^2\Big(\frac{\partial\bar{u}_i}{\partial x_j} + \frac{\partial\bar{u}_j}{\partial x_i}\Big)\\
&\quad - C_2\frac{g}{\theta_0}\Big(f_i\delta_{jz} + f_j\delta_{iz} - \frac{2}{3}f_z\delta_{ij}\Big),
\end{aligned} \tag{9}$$

where the master length scale L is also used for pressure correlation and three more closure constants A_1, C_1 and C_2 are introduced. Similarly, a local balance is assumed for the SFS heat-flux budget,

$$-\frac{1}{3}q^2\frac{\partial\bar{\theta}}{\partial x_i} - \tau_{ij}\frac{\partial\bar{\theta}}{\partial x_j} - f_j\frac{\partial\bar{u}_i}{\partial x_j} + \frac{g}{\theta_0}(\overline{\theta^2} - \bar{\theta}^2)\delta_{iz} + \frac{1}{\rho_0}\Big(\overline{p\frac{\partial\theta}{\partial x_i}} - \bar{p}\,\overline{\frac{\partial\theta}{\partial x_i}}\Big) = 0, \tag{10}$$

where the pressure correlation is given by

$$\frac{1}{\rho_0}\Big(\overline{p\frac{\partial\theta}{\partial x_i}} - \bar{p}\,\overline{\frac{\partial\theta}{\partial x_i}}\Big) = -\frac{q}{3A_2L}(\overline{u_i\theta} - \bar{u}_i\bar{\theta}) - C_3\frac{g}{\theta_0}(\overline{\theta^2} - \bar{\theta}^2)\delta_{iz} + C_5(\overline{u_k\theta} - \bar{u}_k\bar{\theta})\frac{\partial U_i}{\partial x_k}, \tag{11}$$

and where three more closure constants A_2, C_3 and C_5 are introduced.

The stress tensor τ_{ij} appears in the second term and the heat flux f_i in the third term of both Eqs. 8 and 10. This requires Eqs. 8 and 10 to be solved simultaneously for all nine SFS fluxes (six for τ_{ij} and three for f_i), leading to the following expressions for the turbulent fluxes in the MY level-3 scheme,

$$\tau_{ij} = -LqS_M \overline{\frac{\partial U_i}{\partial x_j}} \tag{12}$$

and

$$f_i = \begin{cases} -LqS_H \overline{\partial\theta/\partial x_i} & \text{(for level-2.5 or lower)} \\ -Lq(S_H \overline{\partial\theta/\partial x_i} + \Gamma_\theta) & \text{(for level-3),} \end{cases} \tag{13}$$

where S_M and S_H are non-dimensional stability functions (Nakanishi and Niino 2009). The Γ_θ term represents an upward heat transport in the absence of any local gradient of θ.

Note that the boundary-layer approximation is assumed for Eqs. 9 and 11 in determining S_M, S_H, and Γ_θ; otherwise modelling of the mesoscale limit needs significant changes to include many terms associated with the horizontal differential, and resulting in a significant increase in computational cost. Thus, we decided to determine S_M, S_H, and Γ_θ in the conventional way (Nakanishi and Niino 2009, or see http://www.nda.ac.jp/~naka/MYNN/ where a Fortran program is available).

Nakanishi and Niino (2009) have empirically determined the above closure constants and the master length L based on horizontally-averaged LES results for mesoscale limit applications. We use these closure constants, which are given in Table 1, while S_q and S_θ in Eqs. 3 and 6 are assumed to be $S_q = 3S_M$ and $S_\theta = S_M$. The master length L is determined by a harmonic average of three length scales as

$$\frac{1}{L} = \frac{1}{L_S} + \frac{1}{L_T} + \frac{1}{L_B}, \tag{14}$$

where L_S is given by

$$L_S = kz(1 - 100\zeta)^{0.2}, \tag{15}$$

which is a limit for the unstable surface layer, $\zeta \equiv z/L_M$ is a height scaled by the Obukhov length, $L_M = \theta_0 u_*^3/kgQ$, and u_* is the friction velocity. The second term L_T is defined as

$$L_T = 0.23 \frac{\int_0^\infty qz\mathrm{d}z}{\int_0^\infty q\mathrm{d}z}, \tag{16}$$

Table 1 Closure constants used in Nakanishi and Niino (2009)

A_1	1.18
A_2	0.665
B_1	24.0
B_2	15.0
C_1	0.137
C_2	0.75
C_3	0.352
C_5	0.2

following Blackadar (1962), and the third term L_B is

$$L_B = \begin{cases} (1 + 5(q_c/L_T N)^{1/2}) \dfrac{q}{N} & (\text{for } \partial\theta/\partial z > 0) \\ \infty & (\text{for } \partial\theta/\partial z \le 0), \end{cases} \tag{17}$$

which restricts L due to stable stratification in the inversion layer. Here $N \equiv ((g/\theta_0)\partial\theta/\partial z)^{1/2}$ is the Brunt–Väisälä frequency, and $q_c \equiv (gQL_T/\theta_0)^{1/3}$ is a velocity scale.

3 A Priori Test

The previous section introduced various length scales. Here we investigate how they vary with the non-dimensional filter size Δ_H^* based on an a priori analysis of our benchmark simulations.

3.1 Dissipation Terms

3.1.1 Dissipation Length for TKE, L_ϵ

We apply different filter scales Δ_H^* to the benchmark LES solution at $t = 5$ h (when the PBL depth is about 1500 m) and compute each term in the filtered TKE budget. The four values of non-dimensional Δ_H^* (3.09, 1.25, 0.78, and 0.32) used here correspond to dimensional filter sizes of 201dx (5025 m), 81dx (2025 m), 51dx (1275 m), and 21dx (525 m), respectively.

The vertical profiles of the TKE budget terms are given in Fig. 3. The dissipation rate ϵ is computed from the SGS dissipation term in the LES, which agrees well with that obtained from the residual of other terms in Eq. 2 (not shown). The result for $\Delta_H^* = 3.09$ approaches the mesoscale limit as the profiles are similar to those shown in Fig. 1e. Unlike the production and turbulent transport terms, dissipation varies little with Δ_H^* (Fig. 3a). This is a natural consequence of the TKE cascade; dissipation takes place at a scale much smaller than these filter scales, so the magnitude of dissipation is insensitive to the filter size.

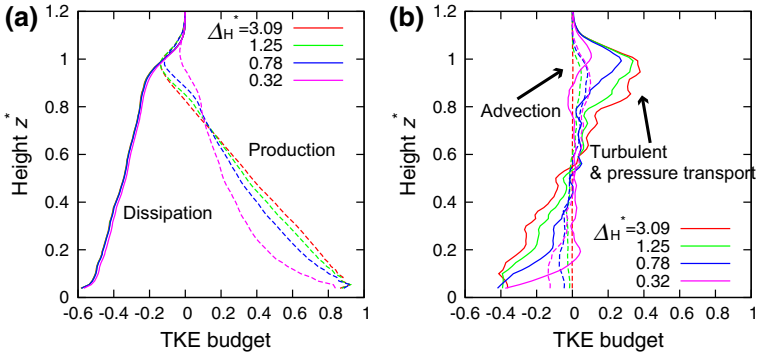

Fig. 3 Vertical profiles of horizontally-averaged terms in the TKE budget equation for four different values of non-dimensional filter size Δ_H^*. In **a**, the *solid lines* represent dissipation and *dashed lines* production, whereas in **b**, *solid lines* are the sum of turbulent and pressure transport, and *dashed lines* are advection. All terms are non-dimensionalized by h, w_*, and Q

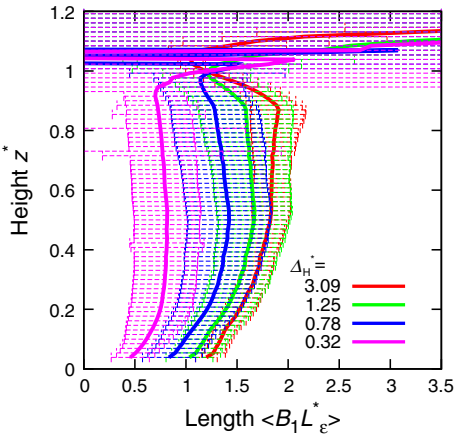

Fig. 4 Vertical profiles of $\langle B_1 L_\epsilon^* \rangle$ for each Δ_H^*. *Error bars* denote the standard deviation of L_ϵ^* at each height

In the TI zone, SFS TKE decreases with decreasing Δ_H^* because more turbulent eddies are resolved. Since the dissipation rate remains nearly the same for various Δ_H^*, we expect the dissipation length scale $L_\epsilon \equiv B_1 L$ in Eq. 4 to depend on Δ_H^*.

Using Eq. 4, together with q and ϵ diagnosed from the benchmark LES, we can compute L_ϵ for various Δ_H^*. Figure 4 shows vertical profiles of horizontally-averaged $\langle L_\epsilon^* \rangle = \langle q^{*3}/\epsilon^* \rangle$ and their standard deviations: first, it shows that $\langle L_\epsilon^* \rangle$ decreases as Δ_H^* decreases. Second, the vertical shapes of all $\langle L_\epsilon^* \rangle$ profiles resemble the profile of the master length $L_\epsilon^*(\infty)$ used in the standard MY model, in which the length increases with height near the surface, becomes almost constant in the middle of the CBL, and then reduces to zero at the top of the CBL (Nakanish 2001; Nakanishi and Niino 2009). Note that the large L_ϵ^* above the CBL shown in Fig. 4 results from very small q and should be neglected. Because the profile shapes are nearly universal, we may assume

$$\langle L_\epsilon^*(\Delta_H^*) \rangle = F(\Delta_H^*) L_\epsilon^*(\infty), \tag{18}$$

where the function F depends only on Δ_H^*.

Figure 4 also suggests that the standard deviation becomes larger for smaller Δ_H^*, implying that $L_\epsilon^*(\Delta_H^*)$ varies more in the horizontal plane as Δ_H^* decreases. We discuss these local fluctuations of $L_\epsilon^*(\Delta_H^*)$ in Sect. 3.1.3. The function F is given below based on the fact that the dissipation rate is independent of filter size,

$$F(\Delta_H^*) = \frac{\langle L_\epsilon^*(\Delta_H^*) \rangle}{L_\epsilon^*(\infty)} = \frac{\langle q^3(\Delta_H^*)/\epsilon \rangle}{q^3(\infty)/\langle \epsilon \rangle} \sim \frac{\langle q^3(\Delta_H^*) \rangle}{q^3(\infty)}, \tag{19}$$

noting that $\langle q^3(\Delta_H^*)/\epsilon \rangle \sim \langle q^3(\Delta_H^*) \rangle / \langle \epsilon \rangle$ is assumed.

We compare our results with an empirical relation derived by Honnert et al. (2011). Based on their analysis, $F(\Delta_H^*)$ is expressed as

$$F(\Delta_H^*) = \left(\frac{\Delta_H^{*2} + (7/100)\Delta_H^{*2/3}}{\Delta_H^{*2} + (3/21)\Delta_H^{*\,2/3} + 3/42} \right)^{\frac{3}{2}}. \tag{20}$$

Figure 5 shows good agreement between this empirical relation and our estimate of $F(\Delta_H^*)$ as $\langle q^3(\Delta_H^*) \rangle / \langle q^3(\infty) \rangle$ based on our benchmark LES with various surface heat fluxes at $z^* = 0.5$. Figure 4 also suggests that $\langle L_\epsilon^*(\Delta_H^*) \rangle / L_\epsilon^*(\infty)$ appears almost uniform, and therefore, it is reasonable to apply Eq. 18 for all heights in the CBL.

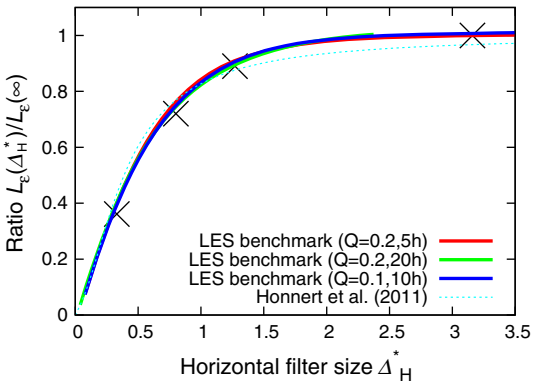

Fig. 5 Ratio of the horizontally-averaged dissipation length scales $\langle L_\epsilon(\Delta^*_H)/L_\epsilon(\Delta^*_H = 3.16 \equiv \infty)\rangle$ computed from Eq. 4 at $z^* = 0.5$ (*crosses*). Estimates from $\langle q^3(\Delta^*_H)\rangle/q^3(\infty)$ from our benchmark LES and the fitting function (Eq. 20; Honnert et al. (2011)) are also shown

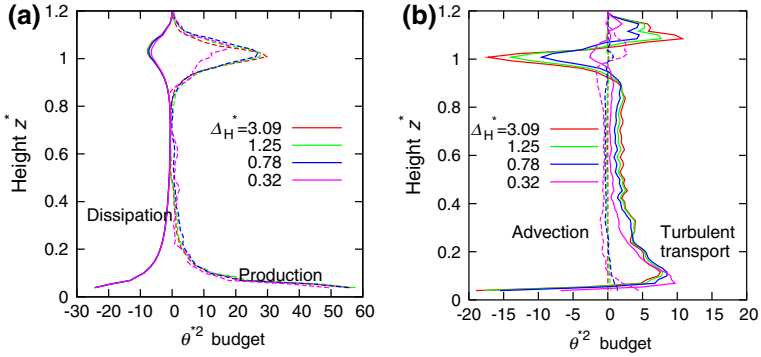

Fig. 6 As in Fig. 3 except for θ^{*2}

3.1.2 Dissipation Length for Temperature Variance, L_θ

We also use the benchmark LES to diagnose each term in the temperature variance budget for various filter scales and display them in Fig. 6, which suggests dissipation varies little with Δ^*_H. Similarly to L_ϵ, we estimated $L_\theta \equiv B_2 L$ from Eq. 7 using the LES-diagnosed SFS q, temperature variance and dissipation rate.

Figure 7 demonstrates that L_θ changes with Δ^*_H in a similar way to L_ϵ. Thus, $\langle L^*_\theta\rangle$ may reasonably be given as

$$\langle L^*_\theta\rangle = F(\Delta^*_H) L^*_\theta(\infty), \tag{21}$$

where the function F is the same as in Eq. 20.[1]

The much larger standard deviations in L_θ (compared with those in L_ϵ) in the mid-CBL are due to a small SFS temperature variance. Again, this large standard deviation suggests the need to look at the local fluctuations of the SFS length scales, which is discussed below.

[1] F presented in Eq. 20 is derived using the partition function for TKE proposed by Honnert et al. (2011). They have proposed another empirical function for θ^2. These functions differ only slightly, so that F is employed in Eq. 21 for simplicity although it is associated with θ^2.

Fig. 7 As in Fig. 4 except for L_θ^*

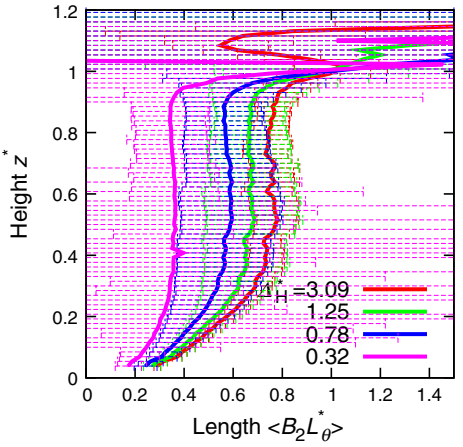

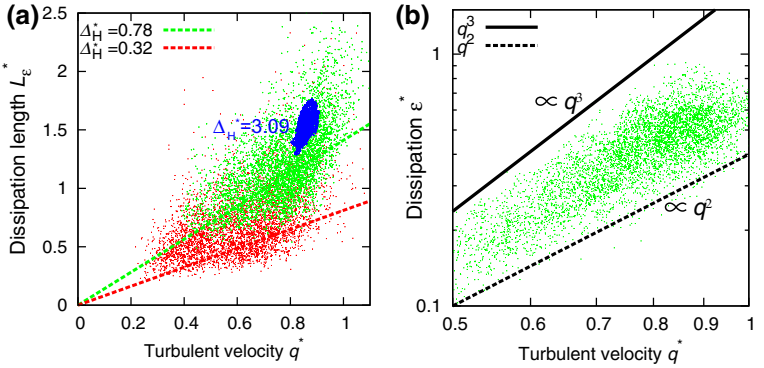

Fig. 8 Correlation between q^* and **a** local dissipation length L_ϵ^* for $\Delta_H^* = 3.09$ (*blue dots*) 0.78 (*green dots*), and 0.32 (*red dots*) at $t = 5$ h and **b** ϵ^* at $\Delta_H^* = 0.78$ on a log–log plot at $z^* = 0.5$. The *green* and *red lines* in **a** represents the fits by the Eq. 22 for $\Delta_H^* = 0.78$ and 0.32, respectively

3.1.3 Locality of Dissipation Length

Here, we discuss local fluctuations of the dissipation length $L_\epsilon(x, y)$ for a fixed Δ_H^* and z. Although L_ϵ can be assumed to be horizontally uniform when Δ_H^* is large enough to rationalize the boundary-layer approximation, its spatial variation increases with decreasing Δ_H^* (Fig. 4 for L_ϵ, and similarly Fig. 7 for L_θ).

Figure 8a shows that the local values of $q(x, y)$ and $L_\epsilon(x, y)$ in the mid-CBL are positively correlated for $\Delta_H^* = 0.32$ and 0.78. In the mesoscale limit ($\Delta_H^* = 3.09$), however, local values are mostly clustered (blue dots). When a local equilibrium holds for TKE, as assumed in LES or the mesoscale limit, $\epsilon \propto q^3$ and hence L_ϵ is independent of q according to Eq. 4. For Δ_H^* at the TI scale, however, the local equilibrium assumption may not be valid. In Fig. 8b, we show that, if $\epsilon \propto q^\alpha$ is assumed, the power α is closer to 2 rather than 3, suggesting that L_ϵ^* may linearly depend on q (according to Eq. 4).

If we assume a linear relationship between local fluctuations of L_ϵ and q as shown by the dashed lines in Fig. 8a, we can express the local length scale as

$$L_\epsilon^*(\Delta_H^*) = \frac{\langle L_\epsilon^*(\Delta_H^*)\rangle}{\langle q^*(\Delta_H^*)\rangle} q^* = \frac{L_\epsilon^*(\infty)}{q^*(\infty)} F(\Delta_H^*)^{2/3} q^* \sim 1.9 F(\Delta_H^*)^{2/3} q^*, \tag{22}$$

where $\langle q^{*3}(\Delta_H^*)\rangle \sim \langle q^*(\Delta_H^*)\rangle^3$. Here we have used Eqs. 18 and 19, and also an empirical relationship $L^*(\infty)/q^*(\infty) \approx 1.9$, which is found at the mid-level of the CBL. This linear relationship between local fluctuations of q^* and L_ϵ^* is shown as the dashed lines in Fig. 8a for the two TI zone filter scales; the lines fit our benchmark data reasonably well. We have also seen a similar relationship for temperature variance,

$$L_\theta^*(\Delta_H^*) = \frac{L_\theta^*(\infty)}{q^*(\infty)} F(\Delta_H^*)^{2/3} q^* \sim 0.8 F(\Delta_H^*)^{2/3} q^*. \tag{23}$$

Including the locality (dependence on q at each grid point) into the length scale should provide a more reliable parametrization of the dissipation. We present the results of an a posteriori test on the performance of parametrizations with and without the locality proposed here, see Sect. 4.

3.2 Parametrization of Third-Order Terms

In the MY scheme, third-order terms such as the turbulent transport and the return-to-isotropy terms in the TKE (Eq. 3) and θ^2 (Eq. (6)) equations need to be parametrized. The conventional MY scheme applies the same master length scale L as that for dissipation to these transport terms. Accordingly, the diffusion length scales introduced in Eqs. 3, 6, 9, and 11 are also given by

$$\langle L^*\rangle = F(\Delta_H^*) L^*(\infty), \tag{24}$$

in the TI zone, where $F(\Delta_H^*)$ is again given by Eq. 20.

To determine the locality of these length scales for third-order terms, we compute each term in Eqs. 3, 9, and 11. Figure 9 shows the correlation between the sum of the vertical pressure and turbulent transport (left-hand side (l.h.s.) of Eq. 3) and $-q\partial e/\partial z$ on the r.h.s. of Eq. 3 for

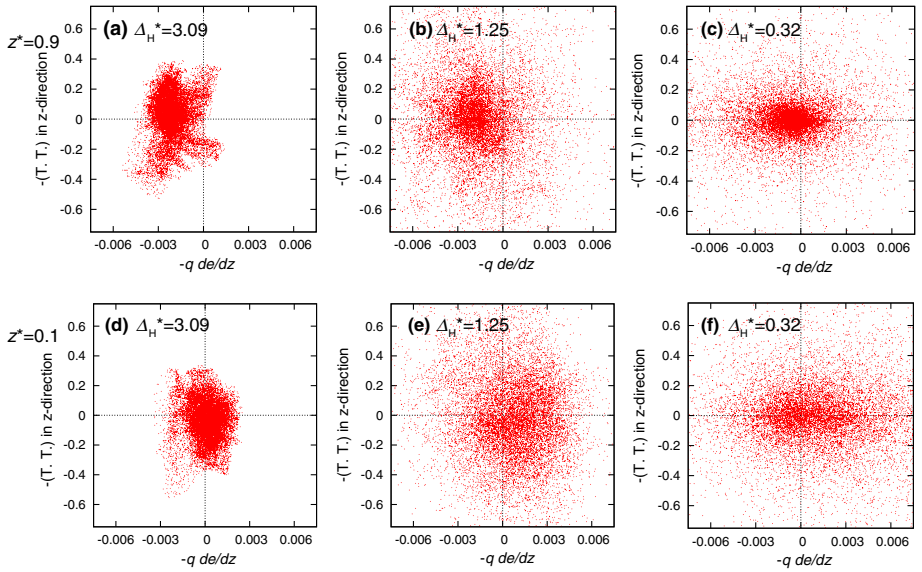

Fig. 9 Scatter plot between the sum of vertical pressure transport and turbulent transport terms in Eq. 3 and $-q\partial e/\partial z$ for various Δ_H^*. The *top three panels* are for $z^* = 0.9$ and the *bottom panels* for $z^* = 0.1$ at $t = 5$ h

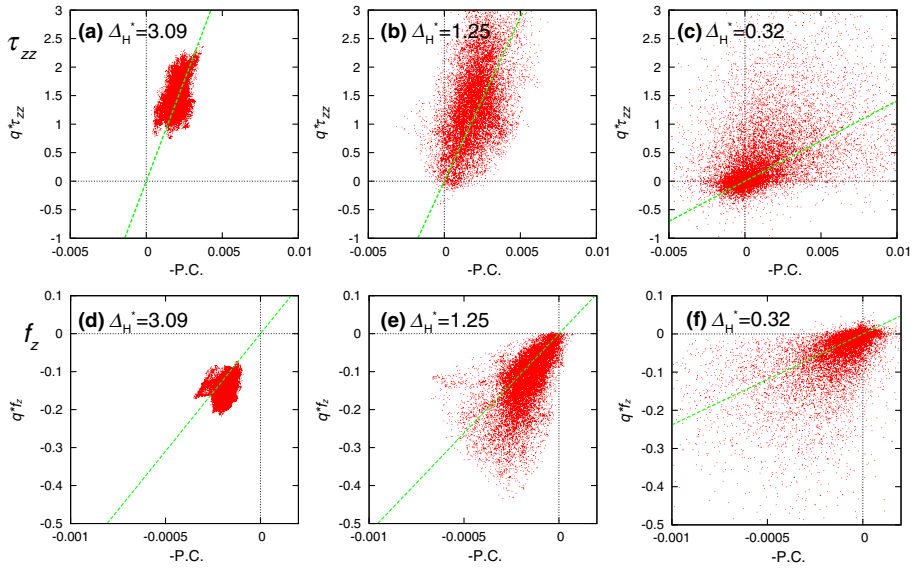

Fig. 10 Correlation between **a**–**c** $-qf_z$ and pressure correlation term (P.C.) of upward heat flux f_z and **d**–**f** $-qf_z$ and P.C. of momentum flux at $z^* = 0.5$ and $t = 5$ h. The *green line* in each panel represents the best fit to $y = ax$

the different values of Δ_H^* and two different z^*. The slopes of a best fit line to the data points in each panel of Fig. 9 would represent the mean length scale $\langle L^* \rangle$. Unfortunately, however, there is much scatter and no clear slope can be derived. The data points that fall in the first and third quadrants indicate down-gradient diffusion, while those in the second and fourth quadrants suggest counter-gradient diffusion. Figure 9 suggests that down-gradient diffusion for local transport is a poor assumption in the TI zone and even in the mesoscale limit in our test. Nonetheless, Fig. 3b (and Fig. 6b near the inversion layer) suggests that the magnitude of the horizontally-averaged SFS turbulent transport decreases with decreasing Δ_H^*. Therefore, it seems reasonable to reduce the horizontally-averaged $\langle L \rangle$ as Δ_H^* is decreased.

Similar issues also arise for return-to-isotropy terms. Our analysis shows large scatter of all return-to-isotropy components, except for the vertical components τ_{zz} and f_z. Figure 10a–c plot the l.h.s. of Eq. 9 against $-q\tau_{zz}$ and Fig. 10d–f the l.h.s. of Eq. 11 against $-qf_z$, at the middle of the CBL, where we assume the rapid terms involving C_1, C_2, C_3, and C_5 to be negligibly small. The reasonably positive correlations in Fig. 10 suggest that there exist meaningful length scales for their pressure correlations, although a small number of points fall in the second and fourth quadrants. Local correlations for other components are so small that no meaningful relations can be deduced (not shown).

From the slopes of best fit lines that pass through the origin in Fig. 10 at each height, we have estimated the horizontal averages of the length scales $\langle L_{\tau_{zz}} \rangle \equiv \langle A_1 L \rangle$ and $\langle L_{f_z} \rangle \equiv \langle A_2 L \rangle$. Figure 11 shows the vertical profiles of $\langle L_{\tau_{zz}} \rangle$ and $\langle L_{f_z} \rangle$ given by the best-fit lines in Fig. 10 for various Δ_H^*. As with the dissipation length (e.g., Fig. 4) these return-to-isotropy length scales decrease with decreasing Δ_H^*.

Local fluctuations in $L_{\tau_{zz}}$ and L_{f_z} still deviate greatly from the horizontal means estimated from the slopes in Fig. 10, particularly in the TI zone. We have tried conditional sampling and correlation analyses with local q fluctuations, but failed to produce any reasonable estimate for the local values of $L_{\tau_{zz}}$ and L_{f_z}.

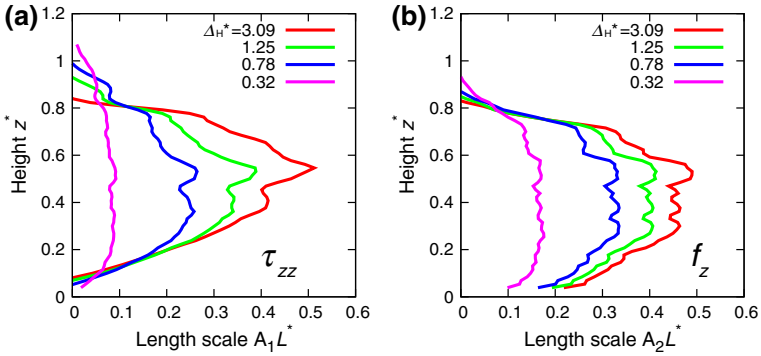

Fig. 11 Vertical profiles of length scales determined by the best fit of correlations for **a** $f_{\tau_{zz}}$ and **b** f_z for each Δ_H^* at $t = 5$ h

The number of samples in our calculation of local SGS statistics, especially the third-order moment statistics, may be of concern. The analysis with $\Delta_H^* = 0.32$ uses only 21×21 data points in computing SGS statistics at each filtered grid, and the large scatter for small Δ_H^* might be due to the small number of samples. In order to address the sampling issue, we have performed another LES with a grid size of 15 m and compared it with the control-run LES. The resulting behaviour of third-order moment SGS statistics is nearly unchanged (not shown). Thus, the sample size does not seem to be responsible for the large scatter.

3.3 Length Scales for Horizontal Turbulent Fluxes

Horizontal turbulent fluxes have been considered insignificant for conventional configurations with a coarse Δ_H^*. When the MY scheme is used in a three-dimensional simulation, a small value of horizontal eddy viscosity is imposed to smooth out the computational noise (e.g., Yamada and Kao 1986). When Δ_H^* falls in the TI zone, however, horizontal turbulent fluxes become significant as shown in Fig. 2b. We expect that a similar modification of a length scale for horizontal diffusion to that in Eq. 24 is necessary in the TI zone. To this end, we also need to obtain a proper length scale for the mesoscale limit $L_x(\infty)$ to parametrize third-order terms of horizontal processes. However, $L_x(\infty)$ has not yet been studied in conventional NWP models.

Ito et al. (2014) investigated the horizontal turbulent diffusivity, $K_H(\infty)$, for the mesoscale limit by analyzing the same LES benchmark data described herein, except that a constant horizontal gradient of a passive scalar $\partial C/\partial y = -1$ was introduced, and an evolution of passive scalar $c = C + c'$ was predicted in the LES. An ensemble-averaged horizontal turbulent flux in the y direction $\langle v'c' \rangle$ at each height gives a vertical profile of horizontal turbulent diffusivity $K_H(\infty)$ and thus the horizontal diffusion length scale, $L_x(\infty)$, in the mesoscale limit can be retrieved as

$$\langle v'c' \rangle = -K_H(\infty)\frac{\partial C}{\partial y} = K_H^*(\infty) w_* h \equiv q^*(\infty) L_x^*(\infty) w_* h. \tag{25}$$

Figure 12 shows the scaled $L_x^*(\infty)$, which turns out to be roughly on the order of 0.1 throughout the CBL. Unlike the length scale for vertical turbulent diffusivity (cf. Degrazia et al. 1997), $L_x^*(\infty)$ does not decrease at the bottom or at the top of the CBL. It may be assumed that the length scales for the horizontal fluxes of momentum and heat are the same as for the

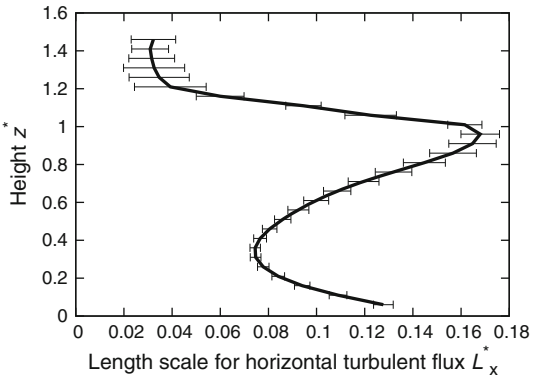

Fig. 12 Vertical profile of length scale $L_x^*(\infty)$ for horizontal turbulent fluxes in the mesoscale limit from Ito et al. (2014)

passive scalar. Thus, a non-dimensional length scale for the horizontal turbulent diffusivity is assumed to be simply $L_x^*(\infty) = 0.1$ with the stability functions set to $S_M = S_H = 1$ for the entire CBL in the mesoscale limit.

We further investigate local fluctuations of the horizontal diffusion length scales based on the τ_{xy} component in Eq. 9. Note that all of the rapidly changing terms are set to zero. As for the vertical diffusion length, the scatter in the relationship between pressure correlation and $-q\tau_{xy}$ (l.h.s. and r.h.s. of Eq. 9) is very large (not shown). We then make a crude assumption that the length scale decreases with the filter size as

$$L_x(\Delta_H^*) = F(\Delta_H^*) L_x^*(\infty), \tag{26}$$

where $F(\Delta_H^*)$ is assumed to be the same form as Eq. 20 for simplicity. This modification, which again ignores large fluctuations, is applied to all horizontal diffusion length scales introduced in Eqs. 3, 6, 12, and 13.

4 A Posteriori Test

An a posteriori test is carried out to investigate the performance of the new MY level-3 scheme with the TI zone modifications described in the previous section. This new scheme is referred to as the TI scheme, and will be compared with the conventional MY scheme.

4.1 Methodology

To test our proposed TI scheme, we use the 3D LES dynamics code described in Sect. 2.1 but with two major changes in the horizontal grid size and the SGS parametrization. The Smagorinsky SGS scheme is replaced by the modified MY level-3 scheme (described in Sect. 2.3) and the SGS length scales are also modified depending on the grid spacing. As in the benchmark LES, the horizontal resolution varies between 500 and 1500 m, while the vertical resolution is fixed at 25 m. The number of grid cells thus varies between 10 and 720 in both x and y directions, and is sufficient to spawn convection cells even for the coarsest dx.

Since a background flow with non-zero wind speed is necessary to properly calculate the stability length L_S in Eq. 15 in the MY scheme, a geostrophic wind speed with uniform vertical shear given by $V = \min(1 + 0.005z, 13.5)$ m s^{-1} is imposed. Unless the horizontal length scale described in Sect. 3.3 is implemented, the SGS horizontal diffusivity is assumed

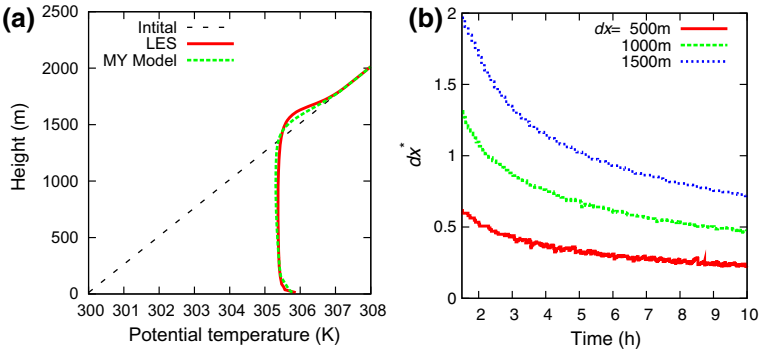

Fig. 13 Results of the conventional MY model run: **a** vertical profile of horizontally averaged potential temperature in the LES and MY level-3 for the mesoscale limit at $t = 5$ h, and **b** time series of $\mathrm{d}x^*$, which is the horizontal grid size scaled by h

to be equal to the vertical diffusivity. To serve as a benchmark, a LES (with grid cell size of 25 m in all three directions) with this geostrophic wind is also carried out. Even with the geostrophic flow, the developed CBL, which has a small friction velocity ($u_* \approx 0.3$ m s^{-1}) and large negative Obukhov length ($L_m \approx -20$ m), can be regarded as a free convection regime (e.g. Wyngaard et al. 1971) and similar to that in the a priori test.

The models were integrated for 10 h, and the results for the initial spin-up period of 1.5 h are excluded from the following analysis. Again, the height of the CBL h is determined by the height at which the vertical gradient of mean $\bar{\theta}$ reaches its maximum.

4.2 The Conventional MY Model Run

We first run the conventional MY model with the same set-up, for comparison with the TI model, where this conventional MY model also uses the same LES dynamical code. The MY model was first tested for a mesoscale limit with $\mathrm{d}x = 100$ km. Figure 13a shows that the vertical profile of potential temperature roughly agrees with the horizontally-averaged potential temperature of the LES.[2]

Now, we reduce the horizontal grid size $\mathrm{d}x$ systematically to 1500, 1000, and 500 m, which all fall inside the TI zone; the non-dimensional grid size scaled by the CBL height $\mathrm{d}x^* \equiv \mathrm{d}x/h$ is used in our analysis. The time evolution of $\mathrm{d}x^*$ is shown in Fig. 13b for the three TI runs, with the simulated $\mathrm{d}x^*$ remaining or becoming <1, which implies that the experiments operate in the TI zone.

The strength of the SGS convection may be evaluated using the ratio $R \equiv e/(e+E)$ at $z^* = 0.5$, where $E \equiv 0.5((u-\langle u\rangle)^2 + (v-\langle v\rangle)^2 + (w-\langle w\rangle)^2))$ is grid-scale or resolvable scale TKE. The ratio R should depend on the grid spacing, approaching a value of 1 in the mesoscale limit because all turbulent motions are SGS motions and should be close to zero in a high resolution LES. Figure 14 shows R for the three TI runs using the conventional MY model; the ratio R always remains larger than 0.9, indicating a small amount of grid-scale convection. These results are compared with those of our LES benchmark simulation (solid curve) retrieved by using various filter widths $\mathrm{d}x^*$. The dashed curve is from a different LES study by Honnert et al. (2011). The conventional MY scheme is found to greatly overestimate

[2] There is a slight difference in the potential temperature profile of the MY model and the LES. This difference can be reduced by using smaller B_1. Since the discussion of the performance of the mesoscale limit is not the purpose of this study, we use the original B_1 value given in Table 1.

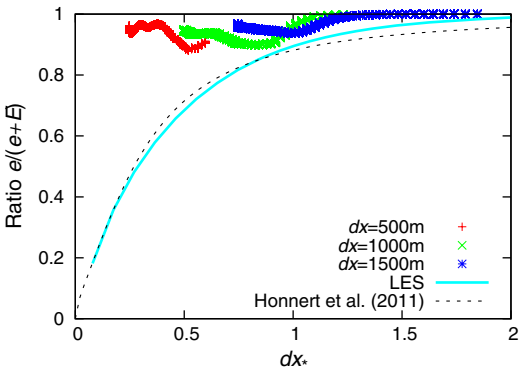

Fig. 14 Ratio $R = e/(e + E)$ for temporally varying dx^* (see Fig. 13b) with three different dx at $z^* = 0.5$. The *solid* and *dashed lines* show R in our LES benchmark filtered by various dx^* and an empirical function suggested by Honnert et al. (2011), respectively

the strength of SGS convection for small dx^* when it is incorporated in a model with a TI scale grid size.

The poor performance of the convectional MY scheme in the TI zone is also seen in horizontal cross-sections of the resolvable vertical velocity field: the vertical velocities of the resolved convection (Fig. 15a, b) are much weaker than those in the filtered LES benchmark flow field (Fig. 15c, d). We also compare the profiles of the grid-scale vertical velocity variances $\langle w^{*2} \rangle$ in Fig. 16. Again, the conventional MY scheme underestimates the grid-scale vertical velocity fluctuations compared with those of the filtered LES.

All turbulent motions are treated as SGS motions in ensemble-mean turbulence models like the MY scheme, so when such models are run at TI scale grid size, no turbulent motions are expected to appear as grid-scale motions under uniform surface heating. However, Zhou et al. (2014) showed that turbulence may erroneously appear as resolvable grid-scale motions when the grid resolution reaches the TI scale. We are attempting to design a TI turbulence model that can bridge conventional ensemble-mean closure models and LES for TI scale simulations. The performance of the TI model is tested against the filtered LES solutions in the next section.

4.3 Performance of the TI Scheme

The length scales in the MY scheme used in the SGS are now changed to those described in Sect. 3. We systematically examine the impacts of each length scale, by their inclusion or exclusion.

Figure 17a shows results when only the dissipation length is modified according to Eqs. 18 and 21 and other length scales are as in the original. Reduction of the dissipation length is found to have the primary impact, inducing stronger grid-scale convection (i.e. smaller R) than the original MY scheme as shown in Fig. 14. Since the net dissipation rate over the entire CBL must remain almost the same for a given buoyancy forcing, the reduced length scale for small dx^* is likely to result in small SGS TKE e. Further, incorporating the length-scale reduction given in Eq. 24 for third-order terms results in similar R as shown in Fig. 17a (not shown). Large temporal oscillations in the entrainment zone are seen in these tests, resulting in the large fluctuation in R.

The inclusion of the TI length scale for all horizontal turbulent fluxes described in Sect. 3.3 has the second largest impact (Fig. 17b). The performance for the TI zone simulations is somewhat improved, because the new horizontal length scale described in Sect. 3.3 does not take into account the stability effect and thus enhances the horizontal diffusivity near

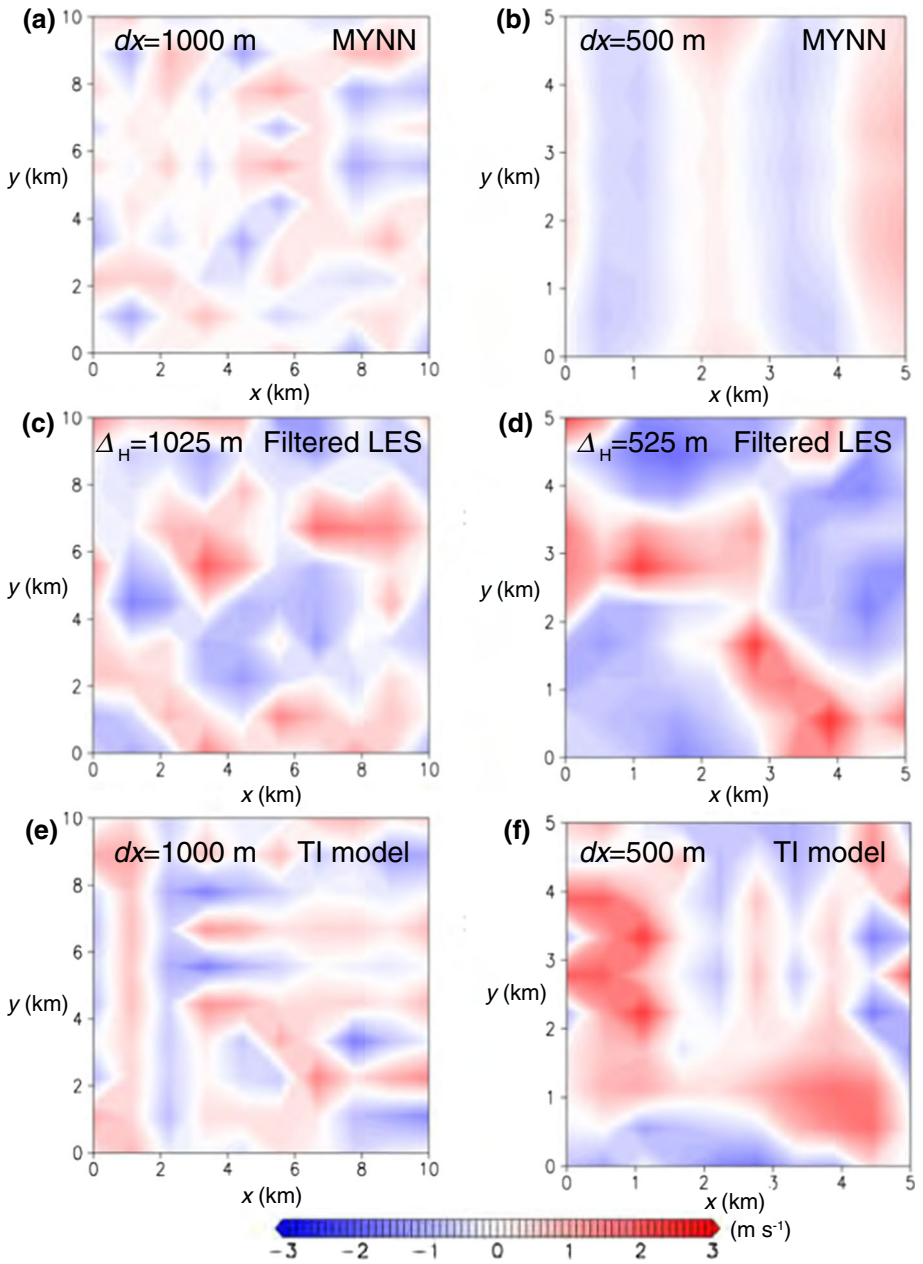

Fig. 15 Horizontal cross-sections of vertical velocity from the conventional MY model for **a** dx = 1 km and **b** 500 m, those from filtered LES for **c** Δ_H = 1025 m and **d** 525 m, and those from the model with the TI scheme for **e** dx = 1 km and **f** 500 m at z^* = 0.5 and t = 5 h

the top of the CBL. The proposed new horizontal diffusion also reduces the large temporal oscillation in the entrainment zone found in simulations using a stability corrected length scale given by Eq. 17.

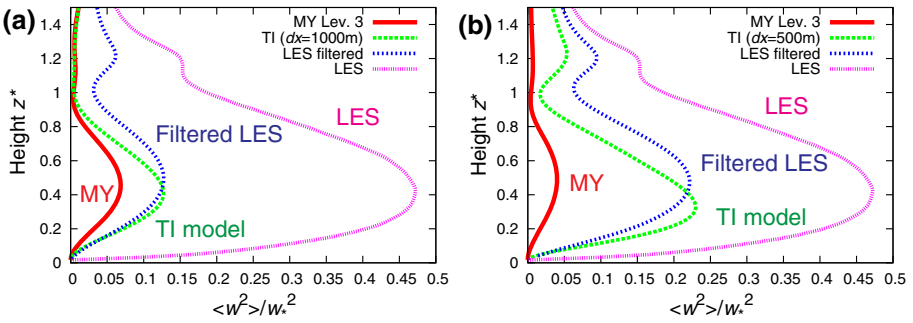

Fig. 16 Vertical profiles of vertical velocity variance $\langle w^{*2} \rangle$ from the LES, the filtered LES, resolved by the TI model, and resolved by the MY model simulations at $t = 5$ h for **a** $\mathrm{d}x = 1$ km and **b** 500 m

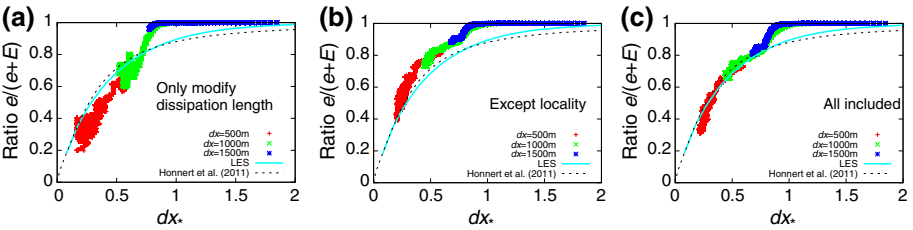

Fig. 17 As Fig. 14 except for the proposed "TI model": **a** only dissipation lengths are reduced by Eqs. 12 and 13, **b** all changes in Sect. 3 except for locality in the dissipation length, and **c** all proposed changes are included

Figure 17c presents the results of implementing all the changes proposed in Sect. 3, including locality (Sect. 3.1.3). Inclusion of the locality intensifies grid-scale convection slightly and hence weakens the SGS TKE. This result agrees best with the benchmark LES analysis. In the following, we show more detailed results from the proposed TI scheme.

Figure 15e and f shows horizontal distributions of the vertical velocity of the convective cells obtained for $\mathrm{d}x = 1$ km and 500 m. The magnitudes of the vertical velocity are comparable to those of the filtered LES benchmark solution (Fig. 15c, d) with corresponding filter sizes of $\Delta_H = 1025$ m and 525 m. The strength of grid-scale convection can be quantitatively evaluated by calculating the resolved-scale vertical velocity variance $\langle w^{*2} \rangle$. Figure 16 shows that the vertical velocity variance for the resolved convection agrees reasonably well with the filtered LES solution for both $\mathrm{d}x = 1$ km and 500 m.

To check the performance for even smaller $\mathrm{d}x^*$, we performed an additional test with $\mathrm{d}x = 250$ m, where the grid is increased to $20 \times 20 \times 200$ to spawn convection cells. The R value in this test agrees very well with that retrieved from the LES (not shown). Therefore, the proposed TI scheme can produce reasonable grid-scale convection for $\mathrm{d}x^*$ as small as 0.1.

5 Concluding Remarks

Based on the LES benchmark for a dry CBL in the free convection regime, we propose a simple extension of the Mellor–Yamada (MY) scheme to a TI zone turbulence simulation. This new TI scheme: (1) modifies various length scales in the conventional MY scheme via

an empirical function that depends only on a scaled horizontal grid size $\mathrm{d}x^*$ (i.e., the grid size normalized by the PBL height); (2) includes a new length scale for horizontal diffusion terms; and (3) incorporates a linear relationship between the local dissipation length scale and local intensity of SGS TKE. Our empirical function is similar to that suggested by Honnert et al. (2011). This extension includes a new length scale to parametrize horizontal turbulent processes but does not change the conventional MY scheme at large $\mathrm{d}x^*$ (i.e., the mesoscale limit). On the other hand, the proposed TI scheme yields similar resolvable versus SGS statistics to the LES solutions for small $\mathrm{d}x^*$. The transition occurs seamlessly. This new parametrization scheme is easy to implement into a NWP model that already employs the MY scheme as a boundary-layer parametrization, and the computational cost of the new TI scheme is almost the same as that of the conventional MY scheme. An a posteriori test shows that a reasonable amount of grid-scale motion is generated mainly because of the reduced SGS TKE dissipation length scale for finer horizontal resolution. Inclusion of horizontal diffusion also improves the simulations.

The major modification of this proposed TI scheme is to the horizontally-averaged length scales. Our LES analysis suggests that fluctuations of local length scales can be very large in simulations with a TI grid scale. The analysis also suggests that a considerable fraction of local diffusion length scales are negative, implying counter-gradient transport, which can be difficult to implement. In this study, we introduce a local relationship between the dissipation length scale and the SGS turbulence intensity, although the inclusion of this locality does not change the overall performance significantly.

A PBL scheme for the NWP of real-world cases must include many complexities that are not addressed in the present study. For example, we did not consider the effect of moisture that can alter boundary-layer characteristics when clouds form in the CBL. We also did not consider the effect of strong vertical wind shear, which often occurs during cold-air outbreaks (Asai 1970), although Shin and Hong (2013) implied that the difference between the free convection regime and a strongly sheared CBL may be insignificant. An ultimate goal is to develop a unified treatment of convection and turbulence (c.f., Mironov 2009) for the TI zone, while another challenging issue is to address horizontal heterogeneity of the land surface, terrain inclination, or synoptic-scale disturbances.

Acknowledgments This work was supported by Field 3, Strategic Programs for Innovative Research, Ministry of Education, Culture, Sports, Science and Technology of the Japanese Government. The computation was conducted using the Fujitsu PRIMEHPC FX10 System (Oakleaf-FX) in the Information Technology Center, The University of Tokyo. We thank three anonymous reviewers for helpful comments.

References

Asai T (1970) Stability of a plane parallel flow with variable vertical shear and unstable stratification. J Meteorol Soc Jpn 48:129–139

Beare RJ (2014) A length scale defining partially-resolved boundary-layer turbulence simulations. Boundary-Layer Meteorol 151:39–55

Blackadar AK (1962) The vertical distribution of wind and turbulent exchange in a neutral atmosphere. J Geophys Res 67:3095–3102

Boutle IA, Eyre JEJ, Lock AP (2014) Seamless stratocumulus simulation across the turbulent gray zone. Mon Weather Rev 142:1655–1668

Businger JA, Wyngaard JC, Izumi Y, Bradley EF (1971) Flux–profile relationships in the atmospheric surface layer. J Atmos Sci 28:181–189

Cuxart J, Bougeault P, Redelsperger JL (2000) A turbulence scheme allowing for mesoscale and large-eddy simulations. Q J R Meteorol Soc 126:1–30

Deardorff JW (1970) Convective velocity and temperature scales for the unstable planetary boundary layer and for Rayleigh convection. J Atmos Sci 27:1211–1213
Deardorff JW (1980) Stratocumulus-capped mixed layers derived from a three-dimensional model. Boundary-Layer Meteorol 18:495–527
Degrazia G, Rizza U, Mangia C, Tirabassi T (1997) Validation of a new turbulent parameterization for dispersion models in convective conditions. Boundary-Layer Meteorol 85:243–254
Eito H, Muroi C, Hayashi S, Kato T, Yoshizaki M (2004) A high-resolution wide-range numerical simulation of cloud bands associated with the japan sea polar-air mass convergence zone in winter using a non-hydrostatic model on the earth simulator. CAS/JSC WGNE Research Activities in Atmospheric and Oceanic Modelling Report, pp 7–8
Hong SY, Noh Y, Dudhia J (2006) A new vertical diffusion package with an explicit treatment of entrainment processes. Mon Weather Rev 134:2318–2341
Honnert R, Masson V, Couvreux F (2011) A diagnostic for evaluating the representation of turbulence in atmospheric models at the kilometric scale. J Atmos Sci 68:3112–3131
Ito J, Niino H, Nakanishi M (2013) Formation mechanism of dust devil-like vortices in idealized convective mixed layers. J Atmos Sci 70:1173–1186
Ito J, Niino H, Nakanishi M (2014) Horizontal turbulent diffusion in a convective mixed layer. J Fluid Mech 758:553–564
Kitamura Y (2015) Estimating dependence of the turbulent length scales on model resolution based on a priori analysis. J Atmos Sci 72:750–762
Leroyer S, Bélair S, Husain SZ, Mailhot J (2014) Sub-kilometer numerical weather prediction in an urban coastal area: a case study over the vancouver metropolitan area. J Appl Meteorol Climatol 53:1433–1453
Mellor GL, Yamada T (1982) Development of a turbulence closure model for geophysical fluid problems. Rev Geophys 20:851–875
Mironov D (2009) Turbulence in the lower troposphere: second-order closure and mass-flux modelling frameworks. In: Interdisciplinary aspects of turbulence. Lecture notes in physics, vol 756. Springer, Berlin, pp 1–61
Moeng CH, Sullivan PP (1994) A comparison of shear-and buoyancy-driven planetary boundary layer flows. J Atmos Sci 51:999–1022
Nakanish M (2001) Improvement of the Mellor–Yamada turbulence closure model based on large-eddy simulation data. Boundary-Layer Meteorol 99:349–378
Nakanishi M, Niino H (2004) An improved Mellor–Yamada level-3 model with condensation physics: its design and verification. Boundary-Layer Meteorol 112:1–31
Nakanishi M, Niino H (2006) An improved Mellor–Yamada Level-3 model: its numerical stability and application to a regional prediction of advection fog. Boundary-Layer Meteorol 119:397–407
Nakanishi M, Niino H (2009) Development of an improved turbulence closure model for the atmospheric boundary layer. J Meteorol Soc Jpn 87:895–912
Ramachandran S, Wyngaard JC (2011) Subfilter-scale modelling using transport equations: large-eddy simulation of the moderately convective atmospheric boundary layer. Boundary-Layer Meteorol 139:1–35
Saito K, Ishida JI, Aranami K, Hara T, Segawa T, Narita M, Honda Y (2007) Nonhydrostatic atmospheric models and operational development at JMA. J Meteorol Soc Jpn 85B:271–304
Shin HH, Hong SY (2013) Analysis of resolved and parameterized vertical transports in convective boundary layers at gray-zone resolutions. J Atmos Sci 70:3248–3261
Shin HH, Hong SY (2014) Representation of the subgrid-scale turbulent transport in convective boundary layers at gray-zone resolutions. Mon Weather Rev 143:250–271
Stull R (1988) An introduction to boundary layer meteorology. Kluwer Academic Publishers, Dordrecht, 666 pp
Wyngaard JC (2004) Toward numerical modeling in the "terra incognita". J Atmos Sci 61:1816–1826
Wyngaard JC, Coté OR, Izumi Y (1971) Local free convection, similarity, and the budgets of shear stress and heat flux. J Atmos Sci 28(7):1171–1182
Yamada T, Kao CYJ (1986) A modeling study on the fair weather marine boundary layer of the gate. J Atmos Sci 43:3186–3199
Zhou B, Simon JS, Chow FK (2014) The convective boundary layer in the Terra Incognita. J Atmos Sci 71:2545–2563